

# A concept for a superconducting tunnelling junction based spectrograph

Mark Cropper,<sup>1\*</sup> M. Barlow,<sup>2</sup> M. A. C. Perryman,<sup>3</sup> Keith Horne,<sup>4</sup> R. Bingham,<sup>2</sup>  
M. Page,<sup>1</sup> P. Guttridge,<sup>1</sup> A. Smith,<sup>1</sup> A. Peacock,<sup>3</sup> D. Walker<sup>2</sup> and P. Charles<sup>5</sup>

<sup>1</sup>*Mullard Space Science Laboratory, University College London, Holmbury St Mary, Dorking, Surrey RH5 6NT*

<sup>2</sup>*Department of Physics and Astronomy, University College London, Gower Street, London WC1E 6BT*

<sup>3</sup>*Research and Scientific Support Department of ESA, ESTEC, Postbus 299, Keplerlaan 1, Noordwijk NL-2200 AG, the Netherlands*

<sup>4</sup>*School of Physics and Astronomy, University of St Andrews, North Haugh, St Andrews, Fife*

<sup>5</sup>*Department of Physics and Astronomy, University of Southampton, Hampshire SO17 1BJ*

Accepted 2003 May 2. Received 2003 May 2; in original form 2002 September 4

## ABSTRACT

We describe a multi-order spectrograph concept suitable for 8-m class telescopes, using the intrinsic spectral resolution of superconducting tunnelling junction detectors to sort the spectral orders. The spectrograph works at low orders, 1–5 or 1–6, and provides spectral coverage with a resolving power of  $R \simeq 8000$  from the atmospheric cut-off at 320 nm to the long-wavelength end of the infrared *H* or *K* band at 1800 nm or 2400 nm. We calculate that the spectrograph would provide substantial throughput and wavelength coverage, together with high time resolution and sufficient dynamic range. The concept uses currently available technology, or technologies with short development horizons, restricting the spatial sampling to two linear arrays; however, an upgrade path to provide more spatial sampling is identified. All of the other challenging aspects of the concept – the cryogenics, thermal baffling and magnetic field biasing – are identified as being feasible.

**Key words:** instrumentation: detectors – instrumentation: spectrographs.

## 1 INTRODUCTION

The scientific case for a medium-resolution spectrograph with high throughput, and which covers both optical and near-infrared, is substantial. A brief résumé would include time-resolved studies of planetary transits, where spectra taken at ingress and egress provide information on the planetary atmospheres;  $\gamma$ -ray bursters, where the spectral evolution during the fading afterglow provides an indication of the interaction of the fireball with its surroundings, and therefore provides information on the progenitor; studies of early structure and pre-galactic clouds through spectra of absorption-line systems in distant quasars; source identifications and redshifts of star-forming galaxies at high redshift detected in submillimetre surveys; supernovae and the interaction between their ejecta and previous episodes of mass loss, leading to estimates of chemical abundances, density distributions and ejecta masses; novae and accreting binary stars, where indirect techniques such as echo and eclipse mapping and Doppler tomography provide detailed information on accretion flows on to neutron stars, black holes and white dwarfs at micro-arcsecond scales; echo mapping of accretion in active galaxies; and in microlensing studies, where detailed information can be obtained on both lensed and lensing objects from the time-resolved spectra. All of these studies require only a small field

of view and a spectral resolving power of  $R > 5000$ ; high time resolution is also important. The coverage of both optical and infrared bands is essential, not only in measuring the spectral energy distribution as it evolves, but also in the relationship between spectral lines at widely different wavelengths, and in the accessibility of the redshifted UV and optical lines in objects at high redshift.

Consequently, one of the instruments identified for a second-generation European Southern Observatory (ESO) Very Large Telescope (VLT) instrument suite was a spectrograph of medium resolving power ( $R \sim 10\,000$ ), with a small field of view (1 arcsec) and spectral coverage over almost a decade in wavelength, from the atmospheric cut-off at 320 nm to the long-wavelength end of the *K* band at 2400 nm. The capability to take relatively short exposures was also cited as important, and the instrument was required to deliver a factor of  $>2.5$  improvement in throughput over current instrumentation. This study was carried out in preparation for a response to the ESO, but not taken further, owing to changes in the manufacturing capability for the detectors.

An increase in throughput by a significant factor over existing front-rank instrumentation is challenging. One improvement is to replace the cross-dispersing grating in a classical echelle with prisms, as in the University College London Echelle Spectrograph (UCLES) at the Anglo-Australian Telescope (Walker & Diego 1985) and the bench-mounted High-Resolution Optical Spectrograph (bHROS) on Gemini (Diego et al. 1997). This should increase the throughput of the cross-dispersing optics by a factor of perhaps 1.5, and also

\*E-mail: msc@mssl.ucl.ac.uk

reduce the polarization effects between dispersing elements suffered in cross-dispersed spectrographs. Alternatively, a non-echelle spectrograph could be feasible, with dichroics splitting the optical into two beams and the infrared into three beams, which is where the detector format is more problematic. This beam-splitting allows the optics and gratings to be optimized for each beam, but is inefficient and allows spectral leakage. Consequently, the overall gains are likely to be modest and such a spectrograph would be complex.

In order to achieve the increased performance required, a radical but optically simple design is needed. We describe such a concept here, a multi-order spectrograph that takes advantage of the intrinsic colour resolution of superconducting tunnelling junction (STJ) detectors. STJs are the first detectors to be able to distinguish colour intrinsically in the UV–IR band (Perryman, Foden & Peacock 1993), and, in their tantalum form, have sufficient wavelength resolution to separate the spectral orders, eliminating the need for order-sorting optics. We calculate that with 5000-pixel linear arrays of STJ detectors, most of the 320–2400 nm range can be covered at a resolving power of  $R \sim 10\,000$  with orders of 1–5 or of 1–6, using a single detector system. The simplicity of the design enables a higher throughput to be reached. STJs have a sensitivity exceeding 70 per cent (uncoated) through most of the optical band. This drops to a few per cent into the infrared, but the coverage of the entire band compensates for the lower quantum efficiency of the detectors.

Because STJ detectors are photon-counting, high time resolution information is preserved. The exposure time can be constructed non-destructively *post facto*, at the data analysis stage. This is particularly important for variable objects, such as  $\gamma$ -ray bursters, where the intensity changes are not predictable beforehand. It also eliminates the overheads of readout time, which can be very large in the case of non-frame-transfer CCDs for short exposure times, especially for echelle formats; this in itself can lead to increases in throughput of factors of up to 2 for short exposures.

A further quality of STJs is that they have no readout noise and insignificant dark noise. Despite the low readout noise of the best current-generation CCDs, this still causes a significant reduction in the signal-to-noise ratio in CCD echelle spectrographs. The gain is particularly marked in the infrared, where current infrared detector technology cannot hope to match the STJ performance in this respect.

Larger format STJ arrays could be envisaged for the future, but to keep within currently feasible technology, we restrict this instrument concept to two linear arrays (the second for sky subtraction). This means that the spectrograph will be optimized for sources of small angular extent, the effective field of view being set by the spatial extent of each pixel. It may, however, be possible to provide some spatial resolution as an upgrade path relatively simply.

Studies (initially by A. Crofts and S. Kahn in the group at Columbia University) for an STJ-based spectrograph working in the UV were presented in the *Hubble STJ (HSTJ)* proposal for the *Hubble Space Telescope* (reported in Jakobsen 1999). A more detailed exposition of this concept here, including a full scientific case, can be found in Cropper et al. (2002).

## 2 INSTRUMENT DESIGN

### 2.1 An overview of STJ detectors

STJ detectors were first developed for the X-ray band, but their potential for use in the UV/optical/IR band was realized by Perryman et al. (1993). They are the first detectors to provide intrinsic colour discrimination at optical wavelengths. This is possible because the

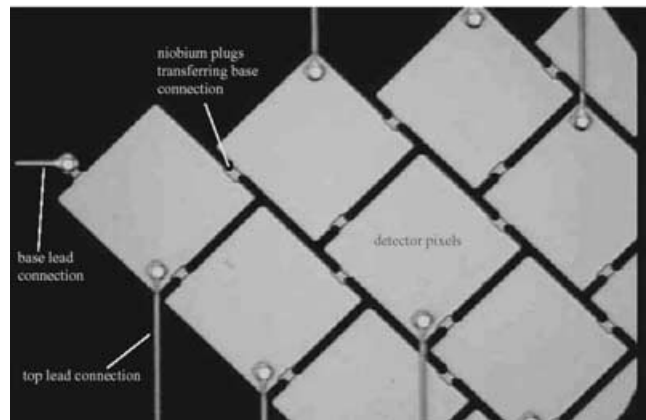
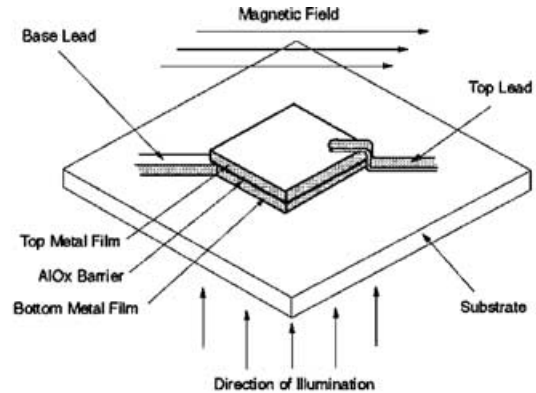


**Figure 1.** A schematic of an STJ pixel (upper panel) and a detailed image of the  $6 \times 6$  tantalum STJ array currently in use in S-Cam2 (lower panel).

energy to break the Cooper pairs in the superconductor is small compared to the energy of an optical photon. The details of the operation of STJs can be found in Perryman et al. (1993), but the essence is that more or fewer electrons are generated, depending on whether the incident photon is blue or red. It then remains to measure this charge, to determine its wavelength.

An STJ consists of two metal films separated by an aluminium oxide barrier, across which the electrons tunnel. This ‘sandwich’ constitutes a pixel. It is supported on a substrate, such as sapphire, through which it is illuminated. Each pixel requires its own electrical connection: generally, the bottom metal film is connected in common with the other pixels, whereas the top metal film has a unique connection. The device requires a magnetic field bias to suppress the Josephson current. A schematic is given in Fig. 1.

Current-generation STJs use tantalum metal films. Pixel sizes range from 20–50  $\mu\text{m}$ . The STJ arrays in the S-Cam2 instrument in use at the 4.2-m William Herschel Telescope at La Palma have a format of  $6 \times 6$  tantalum pixels in a staggered rectangular array (Perryman et al. 2001, and references therein). Each pixel has its own independent pre-amplifier and analogue electronics chain. This array has now been in use for more than two years, and superseded a first-generation array of the same format. S-Cam2 provides a spectral resolving power of  $R \simeq 8$  over the 300–650 nm band. The timing accuracy for the photon events is 5  $\mu\text{s}$  and the maximum count rate is 5000 count pixel $^{-1}$  s $^{-1}$ . A new  $10 \times 12$  pixel array for the camera is under test, and developments using other materials to provide higher intrinsic spectral resolution are under way. Scientific results from S-Cam2 include the determination of quasi-stellar objects redshifts (de Bruijne et al. 2002); studies of the accretion regions and streams

in eclipsing cataclysmic variables (Perryman et al. 2001; Bridge et al. 2002a,b); and observations of the Crab pulsar (Perryman et al. 1999).

## 2.2 Detector constraints

### 2.2.1 Array size and pixel layout

To reach the wavelength coverage required, the spectrograph will need the maximum array length in the dispersion direction. The limits here are set by the wafer size, which we assume nominally to be 5 cm, together with the minimum practical pixel size, 20  $\mu\text{m}$ , giving a maximum length of 2500 pixels. This is insufficient (see Section 2.3), so two such arrays must be butted to give 5000 pixels in the dispersion direction.

Although more than two arrays could be used, thus providing increased wavelength coverage, other aspects (optics and thermal issues) rapidly become more problematic. Because in this concept we have maintained the principle that at most only modest technological developments should be required for the realization of the concept, we reserve such enhancements for the future and limit the array lengths to 5000 pixels.

Yields for current STJ devices are sufficiently high to give confidence that each 2500-pixel strip can be fabricated successfully, so that our concept is feasible. The join region can be made small. Moreover, one of the major difficulties limiting the size of *square* STJ arrays is the access for electrical connections to each pixel: in *linear* arrays this is much easier. Cross-talk between pixels is also lower for the linear arrays because each pixel has half the number of adjacent pixels.

The spectrograph concept assumes a ‘small’ field of view (1 arcsec). The most conservative approach would be to use two strips of detector pixels – one for star and one for sky subtraction, each only 1 pixel wide. This results in a total of 10 000 pixels, each with easy access for electrical connections. This number of pixels is acceptable in terms of electrical connections and signal-processing chains (see Section 2.8). There is some freedom in the width (in the spatial direction) of the pixels. Such rectangular pixels may also slightly increase the intrinsic STJ wavelength resolution without a concomitant increase in array length.

Some spatial information along the slit could be achieved using Distributed Read-Out Imaging Devices (DROIDs). These could be introduced in our concept at a later upgrade path, as their technology matures. DROIDs (Verhoeve et al. 2000) consist of two STJs placed at the end of a tantalum detection strip; the summed charge is related to the energy of the photon, whereas the location at which the photon was detected can be recovered from the difference in the two charges collected by the STJs. Verhoeve et al. (2000) find that  $20 \times 200 \mu\text{m}$  devices provide an effective 11 pixel, for just two electrical connections. The issues here are whether the DROIDs can be laid down efficiently in such large linear arrays, whether their spectral resolution is sufficient for the order separation (this appears to be the case for the spectral formats below), and whether it is more desirable scientifically to have the sky-subtraction array further displaced from the source array than is possible over the effective 11 pixel provided by the DROID.

### 2.2.2 Intrinsic resolution

The key to the spectrograph concept is that the intrinsic wavelength resolution of the STJs is used to perform the order sorting.

Tantalum STJs with 20- $\mu\text{m}$  pixels have a theoretical wavelength resolving power  $\lambda/\Delta\lambda$  of 20 at 320 nm (Peacock et al. 1998), de-

creasing with wavelength to 8.1 at 2400 nm. The resolving power depends on the pixel size: 50- $\mu\text{m}$  pixels have a slightly better resolving power of 22 at 320 nm. In the S-Cam2 array, a practical resolving power of 12 is reached at 320 nm (Rando et al. 2000b), limited by infrared background and electronics noise. (The spectral resolving power of DROIDs is  $\sim 10$ –50 per cent poorer, depending on pixel size – worse for larger pixels.)

Other materials, such as hafnium and molybdenum provide superior spectral resolving power (e.g. Verhoeve et al. 2000), with hafnium exceeding 100 at 320 nm. However, although some junctions have been fabricated from such materials, the technology is not yet sufficiently mature to use in this concept and the spectral resolution of tantalum is, in any case, sufficient.

### 2.2.3 Count rate and time resolution

STJs are photon-counting and intrinsically fast devices. In practice, their time resolution is set by the pulse-counting electronics and the resolution of the time-tagging electronics. In S-Cam, this accuracy is in the regime of tens of microseconds.

The S-Cam2 devices count up to in excess of 5000 count  $\text{s}^{-1}$  pixel $^{-1}$ . The detector resolution degrades slightly with count rate ( $\sim 15$  per cent at 5000 count  $\text{s}^{-1}$  pixel $^{-1}$ ), mostly as a result of pile-up in the currently realized pulse-height analysing electronics (Rando et al. 2000b). Faster count rates would be possible, with revised electronics; however, for this concept we take the approach that the current count rates of 5000 should provide an adequate working count rate limit for sufficient dynamic range.

### 2.2.4 Quantum efficiency

The quantum efficiency of STJs exceeds 70 per cent in the  $U$ – $R$  bands and drops towards longer wavelengths, reaching 20 per cent at 1000 nm and 5 per cent at 2400 nm (see Peacock et al. 1998; Verhoeve et al. 2000). This is mainly the result of reflection off the tantalum film. Other (less well developed) STJ materials, hafnium and molybdenum, have reflective qualities similar to tantalum in the infrared. From the point of view of infrared sensitivity, there are therefore no particular gains to be made from using them.

Potentially, the infrared reflectance can be improved by the deposition of an appropriate coating on the substrate, before the pixel structure is laid down. Currently, little work has been done to investigate this possibility, but this would be obviously desirable for this spectrograph.

The steep drop in quantum efficiency beyond 5  $\mu\text{m}$  in the infrared aids in ensuring that the greater thermal background flux at longer wavelengths does not saturate the detector count rate.

## 2.3 Spectrograph concepts

### 2.3.1 Resolution requirements for order sorting

In order to sort order 2 from order 1, a detector needs to have a resolving power of 2. Generalizing, the highest order a detector can sort is set by the resolving power of the detector at that wavelength.

The increase in order number with decreasing wavelength implies that the resolving power needs to be highest at the extreme blue end of the operating range. The resolution of the STJs increases with decreasing wavelength. This is in the right sense to match the order sorting requirement. In order to minimize the possibility of allocating a photon to the incorrect order, we need some resolution margin  $f_r \sim 1.5$ –2. If we use the current S-Cam2 resolving power of  $\sim 10$ –12 at 320 nm, then, for  $f_r \sim 2$ , the maximum usable

order is 5–6. For these low order numbers, the resolving power required to sort lower orders drops quicker than the intrinsic resolving power of the STJ, so all lower orders can also be sorted (and more easily).

### 2.3.2 Basic constraints from the order sorting

The basic constraints on multi-order spectrographs are simply derived from first principles. We start from the grating equation:

$$m\lambda = d(\sin i + \sin \theta), \quad (1)$$

where  $m$  is the order number,  $d$  is the grating spacing (i.e.  $1/d$  is the number of grooves per unit length),  $i$  is the angle of the incident ray and  $\theta$  is the angle of the diffracted ray. Generally,  $i$  and  $d$  are constant. This indicates that at any position on the detector (implying constant  $\theta$ ) for all orders,  $m\lambda$  is constant. For example, if a particular pixel in order 1 corresponds to 1000 nm, then light from 500 nm in order 2 will also fall on the pixel, 333 nm in order 3, and so on.

If in our case we allow the maximum order to be 5, with a central wavelength of 350 nm, then order 1 will be at 1750 nm. Alternatively, if we wanted a central wavelength of 2100 nm, with coverage down to 350 nm, then the highest order will be 6.

### 2.3.3 Dispersion

The actual wavelength range covered in each order is determined by differentiating the grating equation with respect to wavelength:

$$\frac{\delta\theta}{\delta\lambda} = \frac{m}{d \cos \theta}. \quad (2)$$

Here,  $\delta\theta$  may, for example, correspond to one pixel on the detector. Thus  $\delta\lambda/\delta\theta$  corresponds to the dispersion. We can see that at a particular position on the detector (again, a constant  $\theta$ ), the dispersion,  $\delta\lambda/\delta\theta$ , is proportional to  $1/m$ .

If we calculate the resolving power  $R = \lambda/\delta\lambda$ , then at a particular position on the detector, with  $\lambda = \lambda_1/m$  (where  $\lambda_1$  is the wavelength in first order) and  $\delta\lambda = C/m$  (where  $C$  is a constant), then  $R = \lambda_1/C$ , i.e. constant, independent of order number. Thus although the numerator in  $R = \lambda/\delta\lambda$  is halved, so is the step in wavelength corresponding to, say, 1 pixel. The consequence of this is that all orders have the same resolving power at a particular pixel on the detector.

### 2.3.4 Spectral length

The next step is to calculate the length of the spectrum. *Within* each order, equation (2) indicates that the dispersion is approximately constant if  $\cos \theta$  does not change too much (which is generally true). Thus, within each order, each pixel corresponds to a fixed wavelength interval. Now if we need a resolving power  $R$  corresponding to 2 pixel (for Nyquist sampling of the slit), then the dispersion is given by

$$\delta\lambda = \lambda_c/2R, \quad (3)$$

where  $\lambda_c$  is the centre wavelength of the first order. For example, if we require a resolving power of 10 000 at 2000 nm, this corresponds to 0.2 nm per resolution element, or 0.1 nm per pixel (Nyquist).

The wavelength coverage in each order is then set simply by the number of pixels in the detector. For the above example, a 5000-pixel detector provides coverage in first order of  $5000 \times 0.1 = 500$  nm centred on 2000 nm, i.e. 1750–2250 nm; in second order, it provides  $5000 \times 0.05 = 250$  nm centred on 1000 nm, i.e. 875–1125 nm, and so on. It is evident in this example that there is a gap

between 1125 and 1750 nm not covered by the detector. Gaps can be fixed either by lowering the required resolution or increasing the detector length. Neither of these may be feasible, in which case the location of the gaps has to be optimized.

### 2.3.5 Blaze efficiency

The blaze curve of a grating is approximately unchanged with order if plotted as a function of  $m\lambda$ , instead of  $\lambda$ . The efficiency falls off from the blaze, typically reaching half the peak efficiency at  $(2/3)(\lambda_b/m)$  and  $(3/2)(\lambda_b/m)$ , where  $\lambda_b/m$  is the blaze wavelength for order  $m$ . If we adopt the criterion that the length of each order is defined by the wavelengths at which the efficiency drops to below that of preceding or following orders, then the spectrum appears to shorten gradually as the orders (and thus order overlap) increase. This is familiar from the raw images taken by cross-dispersed echelle spectrographs. It is important to note, however, that some photons will arrive in a particular order beyond this wavelength, and will be there for collection if there are active detector pixels to detect them.

### 2.3.6 Possible configurations

We now apply these considerations with the following inputs: the maximum order is  $\sim 5$ – $6$ , set by the STJ resolving power with factor  $f_r$ ; the minimum wavelength should be the atmospheric cut-off at 320 nm; the resolving power should be  $\sim 10\,000$ ; and the detector length should be limited to 5000 pixels, set by realistic expectations of array size.

We have given an example in Section 2.3.4 above with a resolving power of 10 000. This has gaps between orders for orders up to 4. A reduction in resolving power to 8000 closes the gap between order 3 and 4, and leaves only those between 1 and 2 and between 2 and 3 (only 50 nm around 700 nm in this latter case). Further adjustments can be made in the resolving power and in the centre wavelength of the first order, but if we assume  $\lambda_c(1) = 1750$  nm and  $R(\lambda_c) = 8000$ , then the spectral coverage in Fig. 2 (upper panel) is obtained. This has the advantage of covering the  $U$ – $Z$  bands and the  $H$  band in the infrared.

For a highest order of 6, the centre wavelength of  $m = 1$  is 2100 nm, in the  $K$  band, and we now cover the  $U$ – $R$ , the  $Z$ , the  $J$  and the  $K$  bands, missing the  $H$  and the  $Z$  bands. This is shown in Fig. 2 (lower panel). The wavelengths covered in each band are shown in Table 1.

Exploring further alternatives, if we place order 1 in the  $J$  band, the gap to order 2 includes the  $R$  and the  $I$  bands, which is clearly unsatisfactory. On the other hand, to cover the  $J$ , the  $H$  and the  $K$  bands, the commensurability of their band-centre wavelengths is approximately in the ratio 4 : 3 : 2, so that order 2 should be selected to be at  $\sim 2200$  nm. Unfortunately, this requires a large number of orders,  $\sim 20$  to reach 320 nm, for which an STJ spectral resolving power of  $\sim 40$  would be required. This is out of the reach of tantalum devices, whereas insufficient experience has been gained with other materials such as molybdenum for their use in this concept. This arrangement of orders may be of use in the future.

Of the earlier two possibilities, the first, with  $\lambda_c(1)$  in the  $H$  band, provides optimal and almost complete coverage through the optical band up to the  $Z$  band and complete coverage of the  $H$  band. In the second possibility, where  $\lambda_c(1)$  is in the  $K$  band, an important consideration is the thermal infrared, making this more challenging to realize as a practical design. The loss of some of the  $I$  band may also be undesirable; on the other hand, the  $J$  band is gained. A conservative approach would place  $\lambda_c(1)$  in the  $H$  band, but further

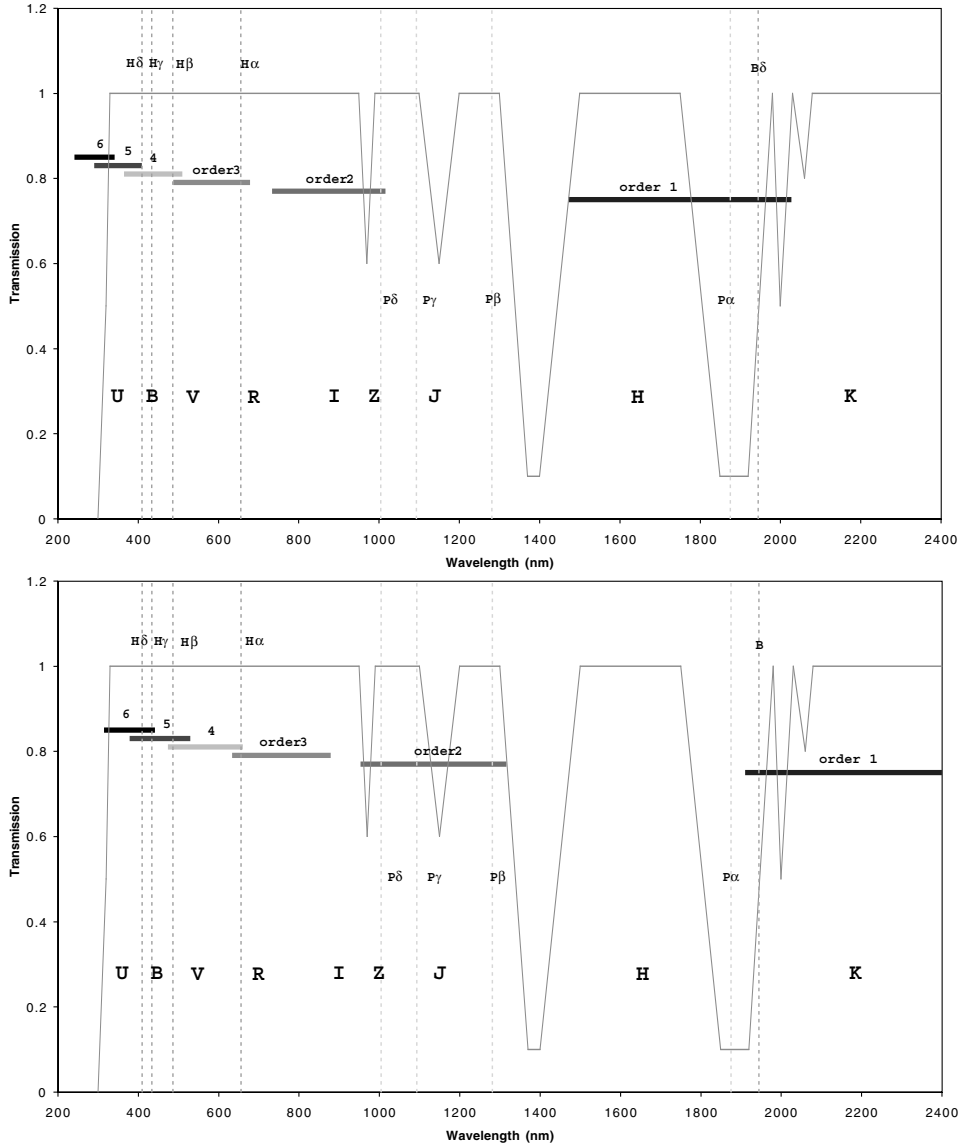


**Figure 2.** The order coverage in the baseline *H*-band configuration (upper panel) and alternative *K*-band configuration (lower panel), together with a schematic depiction of the atmospheric transparency. Also shown are the approximate wavelengths of the *U*–*K* photometric bands and some of the hydrogen Balmer, Paschen and Brackett lines. This figure is available in colour in the online version of the journal on *Synergy*.

consideration may well conclude that the larger infrared coverage provided by  $\lambda_c(1)$  in the *K* band is more scientifically desirable, and also technically feasible.

## 2.4 Optical design

Our optical design concept is relatively simple: a multi-order spectrograph without a cross disperser, using an off-axis collimator and folded Schmidt camera with an accessible focus. The main challenges here relate to the infrared baffling and long wavelength suppression, together with the space required at the focus of the camera for the uniform magnetic field system to bias the STJ array.

Using the principles in Bingham (1979), we have made a preliminary optical layout (Fig. 3). This is based on an off-axis collimator of diameter 261 mm feeding a grating of length 319 mm at an angle of incidence of  $35^\circ$ . The grating has a nominal  $278 \text{ groove mm}^{-1}$ , blazed at  $15^\circ$ . Rays are diffracted at  $5^\circ$  from the grating into a Schmidt camera of a focal length of 655 mm ( $f/2.2$ ), with

a perforated flat-folding mirror to provide access to the focus. The window of the cryostat would be figured to flatten the field, and may need to be achromatic. Optimization is required, particularly regarding the camera back focal distance (currently  $\sim 40 \text{ mm}$ ) to provide sufficient access to the array within the cryostat, and regarding thermal aspects (see Section 2.5).

This preliminary design is relatively straightforward and compact, with the emphasis on being conservative. It may be possible to increase the Nyquist-sampled slit width to match more closely the 0.8-arcsec median seeing typical at most front-rank observatories. This would increase the grating and optics – in particular the camera – and in order to match the fixed detector array size, a faster camera would be required, which will be more difficult. The grating size increase can be limited by immersing it, as in the original HROS concept for Gemini-S (D’Arrigo et al. 2000).

Other concepts are also possible. An all-reflecting camera based on a three-mirror anastigmat (TMA) design may be superior. Off-axis aspheric mirror technology has made significant strides in

**Table 1.** Details of the order coverage provided with a 5000 pixel array, as shown graphically in Fig. 2.  $\lambda_r$  and  $\lambda_b$  are the blue and red extrema of each order, whereas the resolving power is calculated for the central wavelength  $\lambda_c$ .  $\Delta\lambda_c$  is the dispersion in nm pixel<sup>-1</sup> at  $\lambda_c$ . A negative overlap denotes a gap in the spectral coverage.

Order	$\lambda_c$ (nm)	$\Delta\lambda_c$ (nm)	Resolving Power $R_c$	$\lambda_r$ (nm)	$\lambda_b$ (nm)	Overlap (nm)	Overlap (pixel)
1	1750	0.1094	8000	2023	1477	-465	-4250
2	875	0.0547	8000	1012	738	-64	-1167
3	583	0.0365	8000	674	492	14	375
4	438	0.0273	8000	506	369	36	1300
5	350	0.0219	8000	405	295	42	1917
1	2270	0.1419	8000	2625	1915	-603	-4250
2	1135	0.0709	8000	1312	958	-83	-1167
3	757	0.0473	8000	875	638	18	375
4	568	0.0355	8000	656	479	46	1300
5	454	0.0284	8000	525	383	54	1917
6	378	0.0236	8000	437	319	56	2357
7	324	0.0203	8000	375	274	54	2688

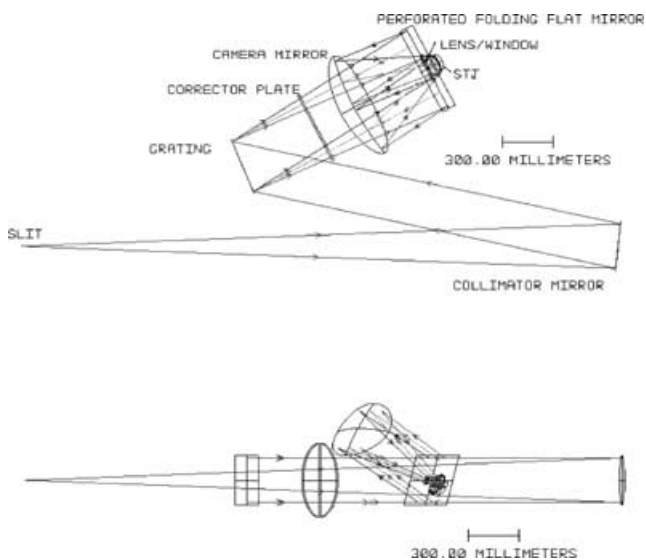


**Figure 3.** Preliminary optical layout. The views are at right angles to each other. Rays are shown for 1477, 1750 and 2023 nm, the centre and extreme wavelengths for order 1. This figure is available in colour in the online version of the journal on *Synergy*.

the past few years and such designs are now routinely being considered.

As a result of atmospheric dispersion, the light from celestial sources is split into spectra, with the blue end pointing towards the zenith. The length of the spectrum is proportional to the tangent of the zenith distance. In a traditional echelle spectrograph at Nasmyth or coudé, a beam rotator is usually used to align the atmospheric dispersion along the entrance slit. The dispersion then adds to, or subtracts from, the cross dispersion. No light is therefore lost at the aperture, although the echelle orders can ‘drift’ slightly on the detector during the process of an observation.

Although losses will be mitigated by using STJ pixels that are rectangular, it will be necessary to consider the effect of atmospheric dispersion. A possible solution uses two counter-rotating fused-silica prisms (‘Risley prisms’) ahead of focus, perhaps with an identical but inverted set near focus. The first prism pair compensates for the atmospheric dispersion and provides a white-

light image in the vicinity of the spectrograph entrance aperture. However, if the aperture were located at this point, the pupil would be displaced in the vicinity of the spectrograph collimator, and it would also be dispersed. If this is not acceptable, a second (inverted) pair of prisms is included, which compensates for both the dispersion and displacement of the pupil in the spectrograph. The overall beam offset created by the two prism-pairs, which varies with zenith distance, is compensated by a telescope offset.

An atmospheric dispersion compensator of any design in the converging beam from the telescope would require an aberration study and may require curved surfaces on the prisms.

## 2.5 Infrared background

Tantalum STJs are sensitive to infrared photons at wavelengths beyond the *K* band. The sensitivity at wavelengths above 1  $\mu\text{m}$  is shown in fig. 8 of Peacock et al. (1998) (curve labelled  $E_T$ ). It decreases to a few per cent at 5  $\mu\text{m}$ , and then drops precipitously, before recovering at wavelengths of greater than 100  $\mu\text{m}$ .

Infrared photons beyond the range of interest have negative consequences as follows:

- (i) the photons generate only small amounts of charge, so – if detected in isolation – they contribute to the electronic noise peak at low pulse heights and may advance the tail of this noise into the first-order peak;
- (ii) because the energy of these photons is small, for a given flux the photon number is high, and the probability of one of these arriving within the time constant of the pulse-counting electronics is high – this adds a small amount of charge which broadens the spectral peak and reduces the resolution;
- (iii) the large photon flux can exceed the maximum count rate of the pulse-counting electronics, leading to saturation of the device; and
- (iv) the infrared photon flux can induce local heating of the detector substrate.

These photons will have been emitted by the source under study as well as the thermal environment of the instrument and cryostat, particularly the warm cryostat window. In S-Cam2, stringent measures were taken to eliminate the infrared flux (Rando et al. 2000a) – first to baffle the field of view seen by the detector, and then to minimize the flux from the cryostat window and baffles by using two filters of successive coldness of KG2 glass. This arrangement depresses the throughput through the optical by  $\sim 40$  per cent, with a turnover at  $\sim 700$  nm, depressing the 1000-nm flux by a factor of  $10^5$ . Nevertheless, the remaining infrared flux is still the major contributor in reducing the spectral resolving power of the STJs from  $\sim 20$  to  $\sim 12$ .

A spectrograph has the advantage over a camera that any flux seen by the spectrograph at wavelengths longer than the red extreme of order 1 will be directed to the side of the detector in the direction of the zero order. This means that the infrared source flux will be less of a problem. However, the thermal loading from the cryostat window will remain, and, indeed, be more significant because of the large window size. In addition, because our concept has an infrared capability, the cut-off of any infrared filter will need to be at wavelengths longer than the red extreme of order 1.

In order to keep the thermal background within acceptable limits, it will be necessary to incorporate the slit and optics grating within a cold environment. This will allow rejection of all source- and window-induced flux. It adds to the cost of the instrument and

influences the cryogenic design significantly, depending strongly on whether  $\lambda_c(1)$  is in the  $H$  band or in the  $K$  band.

One technique for reducing unwanted infrared-flux is to place the detector at the focus of a spherical or toroidal mirror, except for an aperture to accommodate the incoming beam. In this case, the detector experiences a radiated thermal environment approximately appropriate to its surface temperature. This also provides an opportunity for improving the infrared sensitivity: it may be possible to refocus reflected infrared source photons back on to the detector, permitting a second chance for detection. This will require a tilted focal plane, which is not implemented in the initial optical design in Section 2.4.

## 2.6 Calibrations

The calibration requirements are relatively standard, involving detector flat-fielding and wavelength calibration. The infrared night sky lines may be sufficient to provide a continuous monitoring of the wavelength scale for all wavelengths through the superimposed spectral orders on the detector, but external lamps would still be required. A calibration unit would therefore be incorporated, providing an appropriate selection of arc and continuum lamps for the optical and infrared. The flat-fielding will be wavelength-dependent, so filters would be required to isolate a single order for the flat-field calibrations. This would also have a blocked position for checks on the (low levels of) dark noise. The filter unit will be in the main beam so that it can also be used for astronomical observations – for example, should very bright sources be observed in a single order with very high time resolution.

## 2.7 Cryogenics and magnetic field bias

Tantalum STJs operate at a temperature of 0.3 K. This is just within the reach of a pumped  $^3\text{He}$  cryogenic system, but it will probably be better from the point of view of operating costs to use an unpumped  $^4\text{He}$  system, with a final sorption refrigerator stage, as in S-Cam2 (Verveer et al. 1999). Although the STJ array will not, in itself, generate significant heat, the parasitic heat injection through the large harness would indeed be significant. Nevertheless, considerable experience has been gained in the past decade in such cryogenic instrumentation on ground-based telescopes, for example the Submillimetre Common-User Bolometer Array (SCUBA) on the James Clerk Maxwell Telescope on Mauna Kea (0.075 K), and S-Cam2.

### 2.7.1 Cryosystem

Parasitic heat loads on the detector and its cold stage result from radiation from the surroundings, through the support structure for the cold stage and through the electrical cryoharness. The first of these imposes a requirement for nested thermal shrouds. The second requires careful selection of material and strut design. Materials such as Kevlar strings can be considered, but it is likely that stainless steel struts are more satisfactory mechanically, without having too significant a thermal disadvantage.

The mounting of the STJ array to a support structure would require non-magnetic materials with low thermal expansion, in order to match the characteristics of the STJ substrate. Out-gassing in this coldest of environments close to the STJs must also be minimized, as the contaminants will be trapped preferentially on the coldest part of the system, which includes the detector array. The material of choice will probably be a ceramic material. Care will need to

be exercised to interface this structure to the cryocooler cold-finger material.

Significant experience has been gained in the operation of the S-Cam2 cryocooler and improvements have been identified – for example, in the inner surface emissivity optimization, and a reduction in support strut cross-section. This would be valuable in this spectrograph concept, with the main differences being a larger focal plane assembly, a larger magnetic bias system, a larger cryostat window, larger infrared blocking elements, different constraints on back focal distance from the optical design and a very much larger parasitic heat loading through the cryoharness. A particular consideration will be the cooling power of the  $^3\text{He}$  sorption refrigerator.

The other general consideration for the cryosystem is the cooling of the optics, alluded to in Section 2.5. This will entail either the incorporation of the  $^4\text{He}$  cryostat within a liquid nitrogen or other cryostat, or the interfacing of the two cryostats.

### 2.7.2 Cryoharness

For the *HSTJ* studies, we investigated different methods of providing a low thermal conductivity harness through industrial studies (see Griffiths et al. 1997). These included ribbon cables, fine wires, superconducting leads on a ceramic substrate and thin films on a Kapton substrate. It was found that fine wires made from Manganin or stainless steel, or niobium tracks laid on Kapton provided acceptable solutions in terms of electrical conductivity and thermal loading. Surface area, ease of handling and routing, ease of manufacture and ease of making connections were also important considerations, and these favoured the niobium/Kapton solution, which also allowed greater uniformity of the electrical characteristics of the harness (particularly the capacitance). There are a small number of common return lines of lower resistance.

The thermal calculations included the conduction along the tracks and through the Kapton, and included radiative loading and losses. In general, the conduction along the tracks exceeds that through the Kapton. The effect of radiation impinging on the cable at temperatures above 20 K is important, requiring the harness to be covered with a low-emissivity surface such as a gold coating.

The cryoharness must be temperature-clamped on the 4K  $^4\text{He}$  stage in order to limit the requirements on the sorption coolers. In practice, for the spectrograph, the more critical section is the short segment from this stage to the STJ arrays. This would be bump-bonded to make the connection to the STJ detector contacts.

### 2.7.3 Magnetic biasing

A magnet subsystem is required to produce a constant, uniform bias field in the presence of a possibly magnetically noisy environment during the operation of the STJ detectors. It must also be possible to vary the magnetic field during the cooler recycling. This task must be carried out within the restricted accommodation available in the vicinity of the detectors, and operate in conjunction with the thermal infrared filtering and baffling in this locality.

The design of the magnet subsystem depends on the uniformity and stability of the magnetic field required by the STJ detectors. It also depends on the magnetic environment of the STJs; in particular, the presence of motor-driven mechanisms and perhaps compressors in the vicinity of the instrument may impose a magnetically noisy environment with rapid transients. This would drive the magnetic field controller time constants to be shorter.

A design adapted from the pre-proposal studies of the magnet subsystem for *HSTJ* (Griffiths et al. 1997) should be appropriate. This consisted of a screened Helmholtz coil assembly and a set of

magnet power and control electronics. A scaled-down version of this is used in S-Cam2.

The Helmholtz coils are in a  $\mu$ -metal screening box attached to the open end of the cryostat. They operate at superconducting temperature to provide magnetic field bias and trim. Magnetic field sensors are used to monitor the stability and uniformity of the magnetic field.

Control electronics would provide interfaces to the magnetic field sensors in the vicinity of the STJ detectors, control signals for the coil power drive electronics, an interface to the instrument computer and stable and controlled power to the Helmholtz coils.

Particular care will need to be taken with regards to contamination. The STJ detectors would be the coldest elements in the cryostat, so contaminants would be deposited preferentially on them. This would require a careful selection of the materials to be used in the coils and coil assembly, and also some assessment of the likely contamination paths and rates.

## 2.8 Electronics

Each pixel in the STJ arrays requires its own detector chain. The matrix readout approach investigated by Martin et al. (2000) has some performance disadvantages and is not appropriate for the linear arrays required here, so we have retained the approach of providing an independent electronic channel for each STJ element. A 10 000-pixel array therefore needs large-scale integration in order to access these pixels, with analogue electronics of sufficient quality to degrade the detector response minimally. Such a task has been accomplished many times before – for example, in high-energy collider instrumentation and even in space applications [the Burst Alert Telescope (BAT) on the *Swift* satellite; Barthelmy 2000]. Using application-specific integrated circuits (ASICs), each containing  $\sim 100$  channels, a sufficiently low number of circuit cards is needed, so they can be placed close to the detector arrays.

We show in Fig. 4 a block diagram for the data-flow electronics. One hundred ASICs, each providing around 100 pre-amplifiers and analogue-shaping amplifiers, could easily be accommodated on five printed circuit boards. The analogue-to-digital converter (ADC) performance required to convert the amplified charge packets to digital signals is not demanding, owing to the moderate energy resolution of the detectors. An ASIC providing 20 independent 6-bit flash ADCs could easily be developed; 500 of these would be needed and they could be accommodated on 10 printed circuit boards.

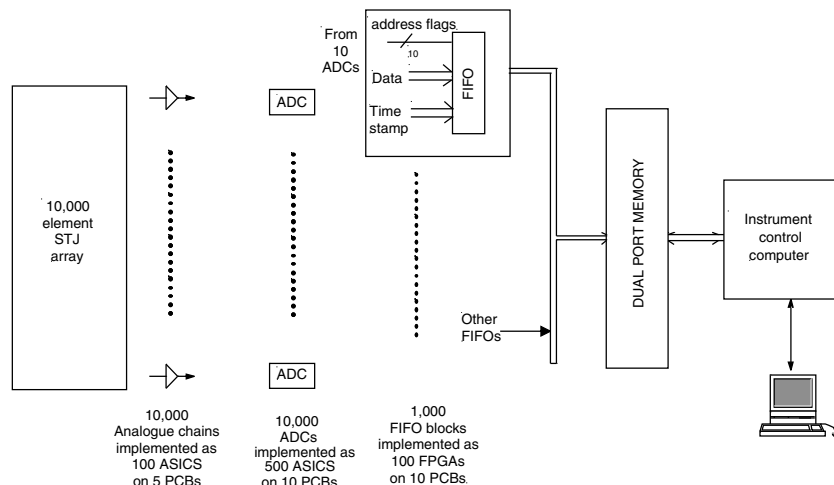


**Figure 4.** The block diagram for the data handling electronics.

These ADCs would operate asynchronously. A small first-in-first-out buffer (FIFO), only a few words deep, could be implemented as a field-programmable gate array (FPGA) to buffer the output from a group of, say, 10 ADCs and record the event time-stamp. We calculate that the event rate in any group of 10 ADCs would not exceed the FIFO write rate. Ten such FIFO blocks could easily be contained within a low-cost FPGA. Each FPGA could also buffer the output from its own FIFOs to provide one output port for onward bussing to a dual port memory, which would be written by the detector system described here. The values written to this memory would be the 6-bit pixel energy, the 14-bit pixel address and a 32 bit time-stamp, which allows 10  $\mu$ s to be resolved per 24 h.

The spectrograph would also require other (relatively standard) instrument electronics to control and monitor the state of the instrument and cryostat, to interface with the observatory and telescope systems and to provide a user interface. Such functions include temperature and magnetic field measurements and field current control, cryogen level sensing, calibration unit activation and control, filter wheel operation, and slit unit control and viewing.

## 2.9 Structure and mechanical issues

We envisage the spectrograph to be situated at the Nasmyth focus. Such an arrangement simplifies the overall structural and mechanical design considerably. Because the gravity vector is constant, flexure issues are eliminated, and the cryostat design is made significantly easier. The spectrograph would be designed around an optical bench structure, on which are mounted the slit unit, the viewing system, the spectrograph optics, the calibration unit and the cryostat. The analogue data handling electronics would be located close to the detector array, with standard interfaces to an external unit containing the majority of instrument control and monitoring electronics and power supplies. Interfaces for replenishment of the cryogenic consumables would also need to be considered.

The major mechanical issue would centre on the thermal performance of the structure, both within the detector  $^4\text{He}$  cryostat and, if present, within the larger cryostat enclosing the spectrograph optics. This is aided by the almost entirely reflective optical design in our concept. Standard techniques (for example, the use of Invar rods) can be used to maintain camera focus between room and cryogenic temperatures.

The slit unit and the slit viewing subsystem are important but standard items; we would not expect these to pose any problems.

The same comment applies to the calibration subsystem. The spectrograph concept would include a filter wheel located between the slit and collimator, which can be used to introduce bandpass, neutral density filters or polarization scramblers, if these are required. These will be useful in commissioning and in calibration; normally, the open position would be used for observations.

### 2.10 Control and data handling software

The spectrograph would need to operate in the host observatory control and data handling system.

It is of fundamental importance that the spectrograph provides real-time feedback, not only on the status of the instrument from its various sensors, but also on the instrument performance directly from the data stream. Outside an observation, use of the calibration lamps should allow detector performance, stability and freedom from electrically-induced noise – and also optical throughput – to be assessed immediately.

STJ detectors produce a photon event stream characterized by time, position and energy. As such, their data outputs are more akin to those from X-ray detectors, so that techniques and tools developed in that field could be the most readily adaptable for this concept. The availability of energy information makes it simpler to retain the event-list format until a final binning in spectral, temporal or spatial coordinates. A data reduction sequence could proceed approximately as described in Perryman et al. (2001). The data volume could be large – up to  $200 \text{ MB s}^{-1}$  – but typically it would be a small fraction of this.

## 3 PERFORMANCE PREDICTIONS

We have developed an instrument simulator to make predictions of the performance of the spectrograph.

As inputs, we use the standard data for Paranal, Chile, available from the ESO exposure-time calculator (ETC) website:<sup>1</sup> telescope UT1 mirror reflectance, sky background brightness, extinction, seeing, infrared absorption. The OH sky-line atlas is from Rousselot et al. (2000), also used in ETC: this extends down only to 624 nm, so misses sky lines at shorter wavelengths. The star spectra are from the atlas of Pickles (1998): these are at 0.5-nm resolution and extend over the 320–2500 nm band of interest.

The simulator interpolates between – or sums over – grids of known transmission, reflectance and emissivity as a function of wavelength, depending on whether the input grid is more finely or more coarsely sampled than that required for the prediction. The throughput is calculated per order, then summed to obtain the overall throughput and signal-to-noise ratios, as well as the total count rate on the array, which is important for ascertaining bright limits.

We limit here the reporting of our exposure estimates to that of the optical+*H* band configuration, but the optical+*J*+*K* configuration can just as easily be calculated.

### 3.1 Throughput

We provide details of the throughput of each element of the spectrograph below the slit for information in Fig. 5. The UT1 mirror reflectivity is for a single reflection – three reflections are used for Nasmyth. The throughputs assume the optical design in Section 2.4, and use polarization-averaged grating efficiencies for appropriate gratings in gratings catalogues. Also shown is the total optical efficiency, excluding and including the slit.

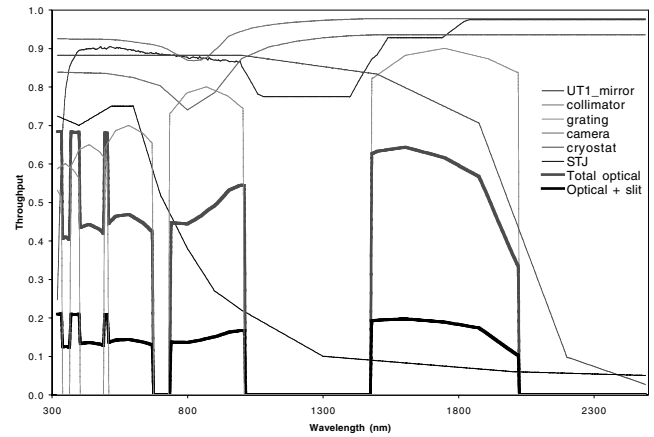


**Figure 5.** The throughput of the individual elements of the spectrograph. The heavy grey curve (red in the online version) shows the total optical efficiency excluding the slit; the heavy black curve includes the slit (0.5 arcsec in 0.8-arcsec seeing, array width 1 arcsec). This figure is available in colour in the online version of the journal on *Synergy*.

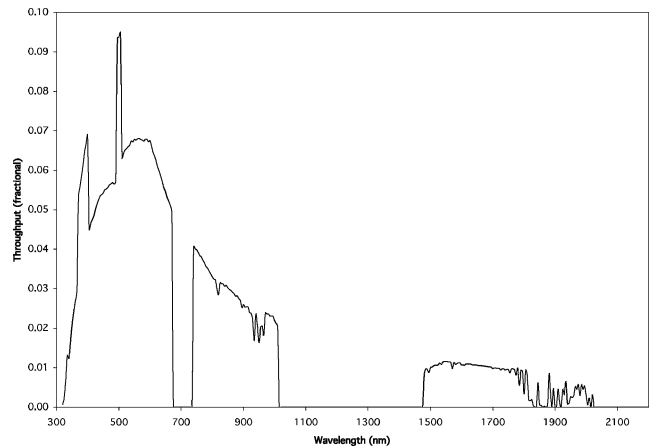


**Figure 6.** The overall throughput of the spectrograph including atmospheric transmission. Peaks occur where there is order overlap on the array.

Fig. 6 shows the overall throughput. The seeing profile is assumed to be Gaussian. The calculations use a zenith angle of  $0^\circ$ , a seeing of 0.8 arcsec, and a slit width of 0.5 arcsec in the spectral direction and 1 arcsec in the spatial direction. The slit is the major source of losses in the spectrograph: the slit transmission is only 0.3 for the above parameters. This is one area where significant improvements may be possible with optimizations of the optical design (see Section 2.4).

### 3.2 Representative spectra

We have calculated star and sky spectra using the throughputs in Section 3.1 above. We show in Fig. 7 the resulting total count spectrum in 1000 s for a  $V = 20$  A0V star; in Fig. 8, we show that for a  $V = 17$  M0V star (both from the Pickles atlas). These spectra are noiseless; signal-to-noise ratio calculations are shown later.

For these calculations, we assume standard zero-points in the literature (Johnson 1966; Bessell 1979), as used in the ESO ETC, and assume the collecting area appropriate for the VLT, as given on the the ESO ETC website. The calculations have been cross-checked against the ESO instrumentation predictions and were found to be consistent to within 20 per cent.

<sup>1</sup> <http://www.eso.org/observing/etc/>

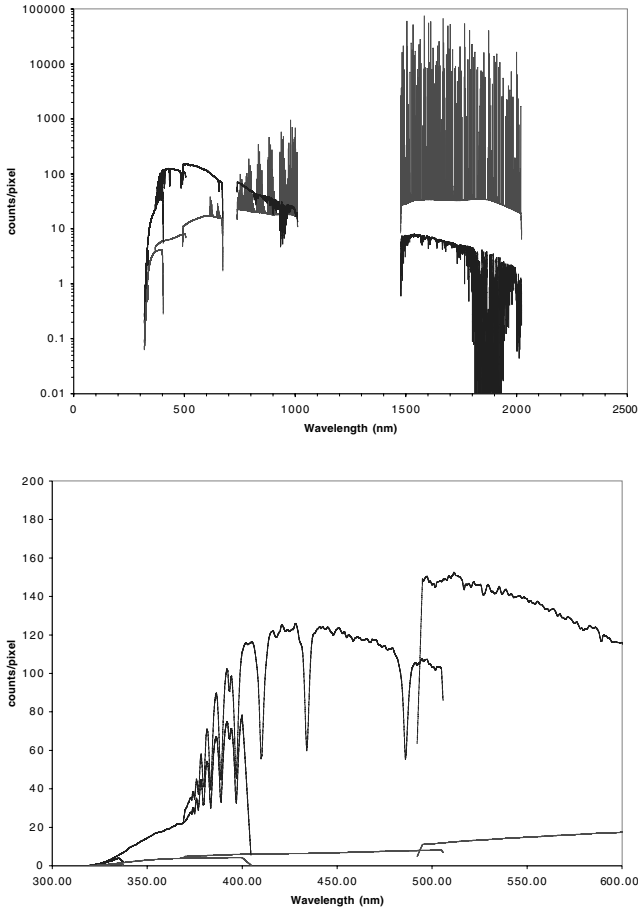


**Figure 7.** The total counts spectrum in 1000 s for a  $V = 20$  A0V star [black (blue in the online version)] and the sky background [grey (red in the online version)], assuming a zenith angle of  $30^\circ$ , seeing of 0.8 arcsec and a slit of 0.5 arcsec. The top plot is on a log scale and shows the full wavelength range, whereas the lower plot on a linear scale shows an expanded region in the blue. This figure is available in colour in the online version of the journal on *Synergy*.

The A0V-star blue continuum dominates the background even for  $V = 20$ ; in the red, the night sky lines are a significant component. These sky lines are seen more clearly in the infrared in the expanded lower plot in Fig. 8, where they are well resolved.

### 3.3 Signal-to-noise ratios

The signal-to-noise ratio calculations use the formulae in the ESO ETC explanatory notes, with the simplification that there is no read-out noise associated with the STJs. We show in Fig. 9 that the spectrograph provides a signal-to-noise ratio reaching  $\sim 10$  per pixel in 3600 s for an A0V star of  $V = 22$ ; it reaches this ratio in the  $H$  band for  $V = H = 18$  in the same time (assuming a seeing of 0.5 arcsec). These figures provide a realistic indication as to the limiting performance at the faint extreme.

Increasing the slit by a factor of 2 increases the throughput through the slit significantly for the typical seeing conditions at Paranal, at the cost of reducing the spectral resolving power to 4000.

### 3.4 Dynamic range

An important aspect of any photon-counting detector system such as STJs is the limit set on the dynamic range by the maximum count rate. This is easier to achieve in a spectroscopic application than in

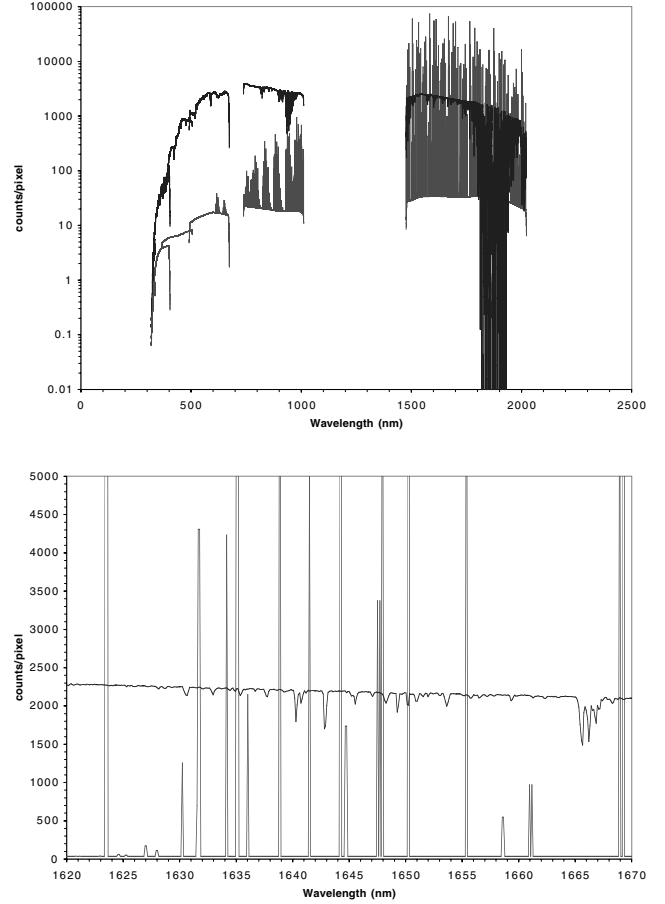


**Figure 8.** The total counts spectrum in 1000 s for a  $V = 17$  M0V star [black (blue in the online version)] and the sky background [grey (red in the online version)], assuming a zenith angle of  $30^\circ$ , seeing of 0.8 arcsec and a slit of 0.5 arcsec. The top spectrum of the full wavelength range is on a log scale, while the lower spectrum, of a short region in the  $H$  band, is on a linear scale. This figure is available in colour in the online version of the journal on *Synergy*.

an imaging application. We show in Fig. 10 the overall count rate (i.e. summed over order number) on the array, as a function of pixel number, for a  $V = 10$  A0V star. The count rates reach  $\sim 3000$  count  $s^{-1}$  pixel $^{-1}$  for such a brightness. The current maximum count rates on S-Cam2 are  $\sim 5000$  count  $s^{-1}$  pixel $^{-1}$ , set by the analogue processing chains. Even if we assume no increase in this capability, this indicates that the spectrograph will have a high bright limit, sufficient for good flat-fielding calibrations (already demonstrated in the case of S-Cam2) and access to celestial spectroscopic standards.

## 4 CONCLUSIONS

We have outlined a spectrograph concept which uses the intrinsic wavelength resolution and extended wavelength response of STJ detectors as the basis for a high-throughput optical–infrared spectrograph with high time resolution. The intrinsic wavelength resolution of the detectors is used to perform the order sorting. Such an STJ-based concept promises an elegantly simple medium-resolution spectrograph. We have calculated that it should be a significant improvement on existing front-rank instrumentation, opening new regions of parameter space.

The concept utilizes technology which is currently available, or can be considered to be feasible with only a small level of development. Nevertheless, it is a step up from existing STJ-based

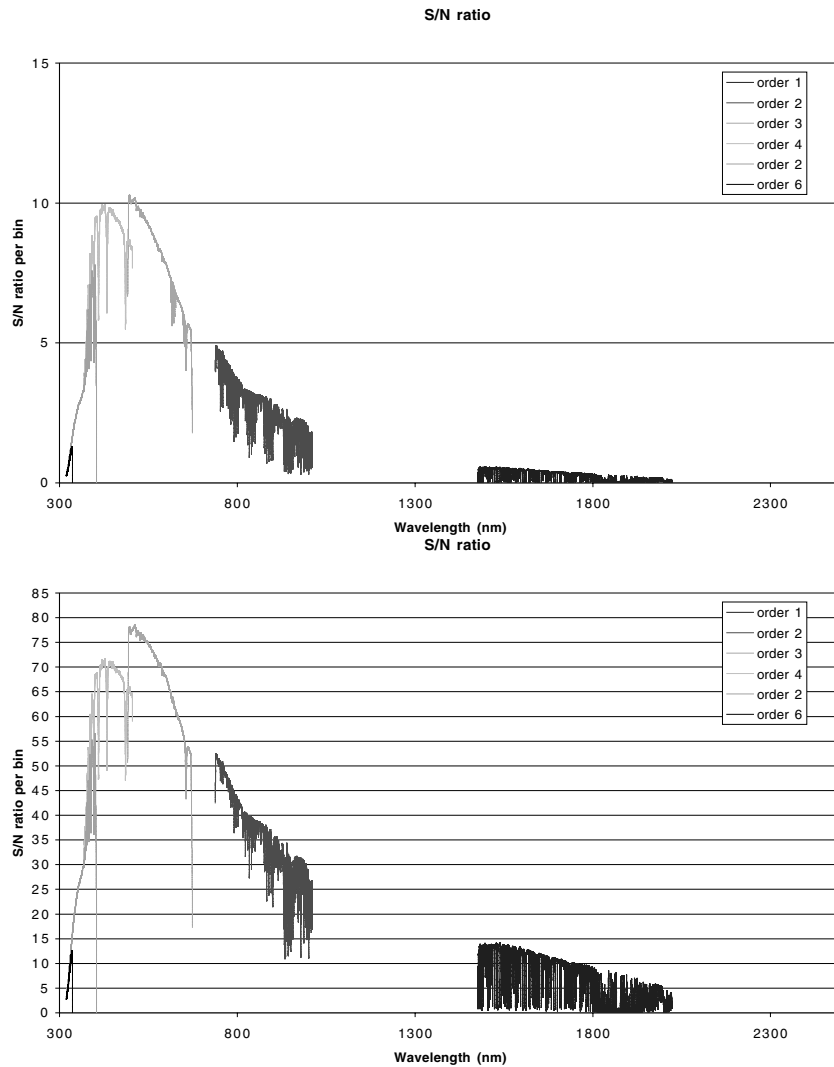


**Figure 9.** The signal-to-noise ratios for a  $V = 22$  (top) and  $V = 18$  (bottom) A0V star in 3600 s. The seeing is 0.5 arcsec, the slit is 0.5 arcsec and the array width is 1 arcsec. The zenith angle is  $30^\circ$ . The different greys (different colours in the online version) indicate different grating orders. This figure is available in colour in the online version of the journal on *Synergy*.

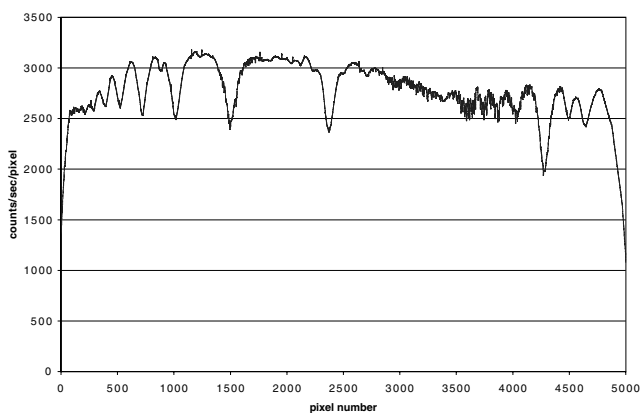


**Figure 10.** The count rate on the detector array ( $\text{count s}^{-1} \text{ pixel}^{-1}$ ) for a  $V = 10$  A0V star. The seeing is 0.8 arcsec with a slit of 0.5 arcsec and an array width of 1 arcsec; the zenith angle is  $30^\circ$ .

instrumentation, in terms of array size and wavelength range. Although we have argued that the technological increment in moving from existing STJ arrays to those suggested for this concept is made

significantly easier by the fact that the arrays in this concept are linear, and so provide for straightforward electrical connectivity, the  $2 \times 2500$  pixel arrays would still be a critical development area. The main challenges are in the area of yield and pixel uniformity (in terms of electrical characteristics). An additional issue is the proximity with which the devices can be butted. Another area closely connected with the detector performance is the subsystem providing the magnetic biasing on the STJ array. The main challenge here is the uniformity of magnetic field bias, given the physically large arrays. At the same time, the cryostat would provide strong constraints in terms of available accommodation for the magnets, the siting of infrared baffles and filters, and the thermal design requirements of the detector support structure.

We have identified further areas where development would be required in the cryocooler and cryoharness. The issue in the former is the heat pumping capacity of the sorption cooler(s) to provide the 0.3 K temperature drop from the  $^4\text{He}$  cryostat. For the latter, the large number of electrical connections to the detector array mean that the parasitic heat loading through these must be minimized. There is also the question of the physical routing of several such cryoharnesses into a relatively small space.

The operation of a 10 000-pixel STJ array is not feasible without large-scale integration of the front-end analogue electronics. This may require dedicated ASICs of particular design suitable for STJs. An ameliorating factor is that the ASICs consist of a large number of relatively simple and independent units.

The infrared baffling and thermal rejection would need careful consideration at the general instrument level (in terms of rejection of telescope thermal background) and for the detector environment, in order to minimize the STJ wavelength resolution degradation, as discussed earlier. It has implications on the overall instrument thermal design, the infrared responsivity, whether the  $\lambda_c(1)$  in the K-band option can be exercised, and ultimately on costs.

On the other hand, we have identified the potential for increased infrared performance by the use of coatings to reduce the reflectivity of tantalum beyond 800 nm, and the appropriate design of the thermal infrared rejection optics around the detector array. A further performance enhancement may be available through the provision of a degree of spatial resolution along the slit by the use of DROIDS.

## ACKNOWLEDGMENTS

Support for the STJ technological development at ESA-ESTEC is provided by Peter Verhoeve, Nicola Rando, Didier Martin, Jacques Verveer and Axel van Dordrecht. Keith Horne is supported by a PPARC Senior Fellowship.

## REFERENCES

- Barthelmy S., 2000, SPIE, 4140, 50  
 Bessell M. S., 1979, PASP, 91, 589  
 Bingham R. G., 1979, QJRAS, 20, 395  
 Bridge C. M. et al., 2002a, MNRAS, 336, 1129  
 Bridge C. M., Cropper M., Ramsay G., de Bruijne J. H. J., Reynolds A. P., Perryman M. A. C., 2002b, MNRAS, 341, 863  
 Cropper M. et al., 2002, Proposal submitted in response to ESO AO for second-generation VLT instrumentation, SES/MSSL/PR/0001.01 (contact msc@mssl.ucl.ac.uk)  
 D'Arrigo P., Bingham R., Charalambous A., Crawford I., Diego F., Percival J., Savidge T., 2000, SPIE, 4098, 159  
 de Bruijne J. H. J. et al., 2002, A&A, 381, L57  
 Diego F. et al., 1997, SPIE, 2871, 1126  
 Jakobsen P., 1999, in Morse J. A., Shull M. J., Kinney A. L. eds, ASP Conf. Ser. 164, UV-Optical Space Astronomy Beyond HST. Astron. Soc. Pac. San Francisco, p. 397  
 Johnson H. L., 1966, ARA&A, 4, 193  
 Martin D., Verhoeve P., Peacock A., Goldie D., 2000, SPIE, 4008, 328  
 Peacock A., Verhoeve P., Rando N., Erd C., Bavdaz M., Taylor B. G., Perez D., 1998, A&A Suppl., 127, 497  
 Perryman M. A. C., Foden C. L., Peacock A., 1993, Nuclear Instrum. Methods Phys. Res., A, 325, 319  
 Perryman M. A. C., Favata F., Peacock A., Rando N., Taylor B. G., 1999, A&A, 346, L30  
 Perryman M. A. C., Cropper M., Ramsay G., Favata F., Peacock A., Rando N., Reynolds A., 2001, MNRAS, 324, 899  
 Pickles A. J., 1998, PASP, 110, 863  
 Rando N., Verhoeve P., Gondoin P., Collaudin B., Verveer J., Bavdaz M., Peacock A., 2000a, 8th International Conference on Low Temperature Detectors, Nucl. Instrum. Methods Phys. Res. Sect., A, 444, 457  
 Rando N. et al., 2000b, SPIE, 4008, 646  
 Rousselot P., Lidman C., Cuby J.-G., Moreels G., Monnet G., 2000, A&A, 354, 1134  
 Verhoeve P., den Hartog R., Martin D., Rando N., Peacock A., Goldie D., 2000, SPIE, 4008, 683  
 Verveer J., Rando N., Andersson S., Gondoin P., Peacock A., 1999, Rev. Sci. Instrum., 70, 4088  
 Walker D., Diego F., 1985, MNRAS, 317, 255

This paper has been typeset from a  $\text{\TeX}/\text{\LaTeX}$  file prepared by the author.